https://doi.org/10.3311/PPci.43289

Periodica Polytechnica Civil Engineering, 70(2), pp. 395–410, 2026

Video-based Analysis and Damping Identification of a Ball Absorber on a Circular Rail Track

Marek Kawulok[1,2*], Stanislav Pospíšil[1,2]

[1] Department of Structural Mechanics, Faculty of Civil Engineering, VSB-Technical University of Ostrava, Ludvíka Podéště 1875/17, 708 00 Ostrava-Poruba, Czech Republic
[2] Institute of Theoretical and Applied Mechanics of the Czech Academy of Sciences, Prosecká 809/76, 190 00 Prague 9, Czech Republic
[*] Corresponding author, e-mail: marek.kawulok@vsb.cz

Received: 07 January 2026, Accepted: 01 April 2026, Published online: 22 April 2026

Abstract

This paper investigates the dynamic behaviour of a rolling ball absorber moving along a circular track whose surface is formed by a pair of rails. The rail geometry constrains the motion of the ball to a planar trajectory. Experimental measurements of free oscillations are recorded using a video camera and subsequently processed by a presented algorithm. The output of the algorithm is the angular displacement of the absorber ball as a function of time. The free-vibration response is further analysed by fitting a numerical simulation to the experimentally obtained time history. The equations of motion are derived for a physical model consistent with the experimental setup and include a combination of viscous damping and rolling resistance to describe energy dissipation. The fitting procedure aims to identify an optimal combination of viscous and rolling damping coefficients that yields the best agreement between the numerical simulation and the experimental response.

Keywords

ball vibration absorber, motion tracking algorithm, experimental measurements, numerical simulation, damping

1 Introduction

Vibration damping of structures is one of the major and because of its complexity least explored fields of structural dynamics. It aims to reduce vibrations, which may have a significant impact on the structure and the comfort of the occupants. In the extreme case, the vibration causes the structure to collapse or be damaged, with consequent hazards to the occupants. Vibration also causes discomfort for people dwelling in a vibrating building or on the footbridge when certain acceleration thresholds are exceeded [1, 2]. Structural engineers are responsible for designing vibration-resistant building structures with a focus on structural efficiency. The key to an effective design is to maximize the efficiency of the structure while minimizing material demand. This effort contributes significantly to the economic efficiency and sustainability of civil engineering projects [3].

A feasible solution to reduce the effect of vibrations on the structure is the implementation of damping devices. The most robust and widely used type are passive absorbers, including so-called tuned mass dampers. These systems are characterized by the fact that they do not require an electrical power supply to operate. Instead, they use the movement of the main structure itself to trigger its effect [4]. and dissipate of energy that is introduced into the structure by external sources [5].

One particular representative of this group is the ball vibration absorber, which consists of two components, namely a support ball and an inner ball. The absorber is used, for example, in tall, slender buildings or long linear structures, mainly because of its robustness (as mentioned above) and relatively small dimensions. However, there are also difficulties associated with the inherently nonlinear nature of this system. These are mainly associated with motion auto-parametric oscillations and instabilities [6]. The nonlinear nature of the system makes the response strongly dependent on the amplitude of external excitation, as it has been shown with numerical calculation [7, 8]. These simulations are able to provide valuable information about the behavior of a dynamic system described by equations of motion, however, some simplifications have to be made during their derivation.

Cite this article as: Kawulok, M., Pospíšil, S. "Video-based Analysis and Damping Identification of a Ball Absorber on a Circular Rail Track", Periodica Polytechnica Civil Engineering, 70(2), pp. 395–410, 2026. https://doi.org/10.3311/PPci.43289

Moreover, it is often required to validate the results obtained experimentally and vice-versa.

Several publications that contain an experimental part address the topic of the spherical absorber [9–13]. Two categories can be distinguished here, namely the experimental measurement of the response of the supporting structure and the monitoring of the response of the ball. The first category includes studies, such as [9], where the experimental portion of the article focuses on analyzing the response of a structure equipped with a planar model of a ball absorber. The structure was subjected to free vibration, harmonic, and seismic excitation. In [10], the response of a wind turbine model without a damping device and with a spherical absorber was analyzed. Experiments were also conducted on the wind turbine model described in the publication [11] to analyze how the structural response changes with the varying number of balls placed in the support bowl. As a representative of the second category of experimental measurements, we can include, for example, [12, 13]. In [12], ball displacements are measured using relative displacement sensors. In this work, the author analyzes the absorber response along with the logarithmic decrease in damping with the application of different rolling surface materials and the vibration absorption efficiency. The author's team adopted a different approach to measuring the response, following the method used in [13], where video recordings were employed to capture the ball's position. In these experiments, the camera was placed over the bowl and the deflection in one direction was traced. The video was captured at 25 frames per second and MATLAB Image Processing and Computer Vision Toolbox [14] was used for the processing.

This article presents a procedure for analyzing the response of a rolling ball absorber whose motion is constrained to a planar trajectory by a circular two-rail track. Free oscillation experiments were carried out using a specially designed experimental setup, while the system response was measured in a fully non-contact and non-intrusive manner. The motion of the ball was captured exclusively by video recordings, without the use of any additional sensors or measuring devices attached to the system, thereby ensuring that the physical nature of the phenomenon was not affected. This measurement strategy provides a clean and unobstructed observation of the system dynamics, which is particularly advantageous for lightweight or highly sensitive structures. An image-based algorithm was then applied to the recorded videos to extract the time history of the ball position, which was subsequently converted into angular displacement during post-processing.

Based on the experimentally obtained response, a physical model of the system was formulated using equations of motion that include both viscous damping and rolling resistance. The parameters of the damping model were identified by fitting numerical simulations to the experimentally observed decay of oscillation amplitudes. The results demonstrate that the proposed approach provides a consistent and physically interpretable description of the dissipative mechanisms governing the free oscillations of the ball absorber.

2 Experimental setup

The experimental setup consists of a steel structure that serves as a base and a support structure equipped with a path for the ball rolling motion. In the case of a ball absorber, the support structure is a bowl. Although the experiments described below restrict the motion to a planar trajectory, the term 'bowl' is used for the support structure for the sake of concise terminology. The steel base is made up of two U-profiles that are connected by a tube. The top of the structure is equipped with two rails on which the "trolley" moves. The trolley is secured on the rails by three pairs of wheels that hold the rail to ensure stability and precision of movement. The trolley itself is then made up of two steel plates interconnected by a pipe (the diameter is much smaller than the pipe used for the base). The dimensions of these plates differ, since one of them is used to fix only one pair of wheels, while the other has two pairs of wheels attached and serves to secure the position of the bowl. A schematic model of the steel base and trolley, with a description, is shown in Fig. 1. This steel base equipped with a trolley has already been used for experimental measurements of pendulums with viscous dampers [15, 16].

Bowl parameters were designed based on numerical simulations such as those found in [8]. The bowl consists of two

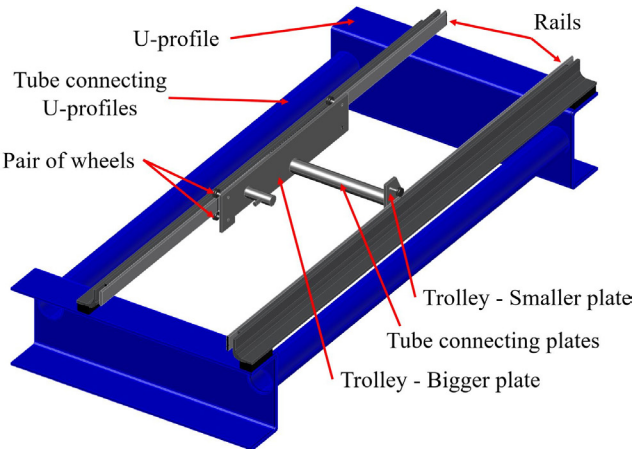

Fig. 1 Schematic model of the steel base and trolley with description

glued wooden plates, which have a modified shape and serve as tracks for rolling motion. Each of the glued plates consists of three thin wooden plates of 2 mm thickness layered on top of each other. The only difference between the layers is the diameter of the curvature of the rolling track. This offset was chosen to create a stepped edge on which a rubber pipe could be mounted to increase friction (see Fig. 2). The radius of curvature is 206, 204 and 200 mm, respectively. This means that without the rubber pipe, the rolling path has a radius of 200 mm. The glued wooden plates are interconnected by threaded rods. Spacers are inserted between the plates on the threaded rods to ensure equal spacing at each point. By using spacers of different lengths, the spacing of the boards can be modified according to the requirements of the experiment. The 3D model of the bowl can be seen in Fig. 3.

The completed bowl is placed on the tube that connects the steel plates of the trolley (see Fig. 4). Several enhancements have been made to achieve an efficient connection between the trolley and the bowl, including a laser-prepared cutout to ensure proper load transfer in the direction of movement. Other components providing rotational rigidity are bolts fitted into pre-prepared holes on one of the plates

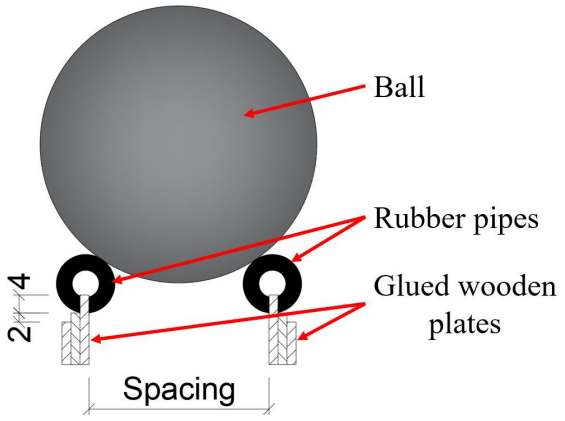

Fig. 2 Schematic drawing of the ball on the track with rubber pipes

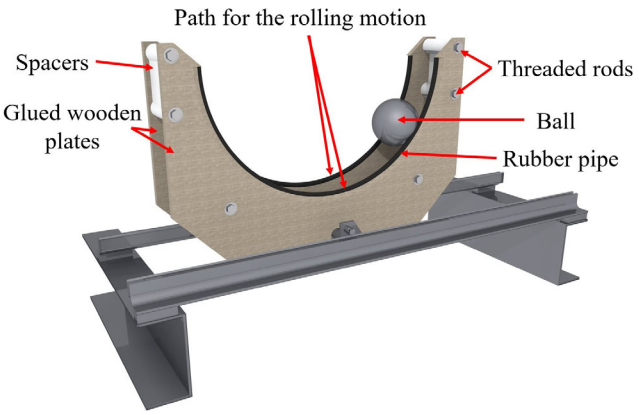

Fig. 3 Schematic model of bowl with description

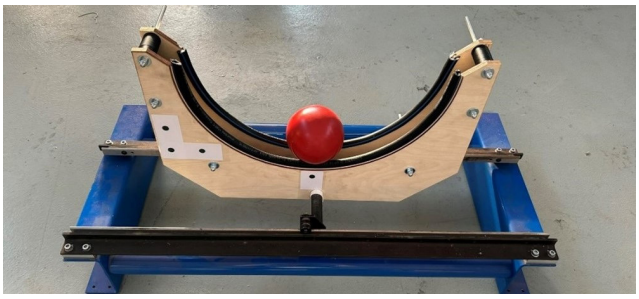

Fig. 4 Photograph of the assembled experimental device: The reference points that can be seen on the wooden plate were created using a 3D printed template

and connected to the trolley. Some of the elements, such as spacers or templates for creating reference points, are created using 3D printing technology. The reference points (see Fig. 4), which are created on the surface of the bowl using templates, are used in the algorithm to convert the results from pixels to millimeters.

The video footage of the experiment was taken on a mobile phone at a resolution of 1920 × 1080 progressively displayed pixels (fullHD). The frame rate was set at 120 frames per second. The mobile phone was mounted on a tripod and positioned so that the experimental setup remained fully visible in the frame during oscillations.

3 Obtaining results from a video recording

Section 3 will describe the procedure for analyzing the video footage taken during the experiment. The outcome of the analysis is the position of the center of the sphere in time. In this study, the procedure is applied to free oscillations. It should also be noted that in the algorithm for the tracking of the ball, there is also the tracking of reference points. All objects whose centers are tracked in the algorithm will generally be called tracked objects.

3.1 Determination of camera parameters

It is necessary to determine the camera parameters that are essential to remove image distortion before starting to work with the video. To obtain the parameter, one of the MATLAB Image Processing and Computer Vision Toolbox [14] tool is used, namely Camera Calibration [17]. This application includes *EstimateCameraParameters* functionality (see [18]). Using this functionality, it is possible to estimate the intrinsic matrix, which is part of an equation that provides a relation between the coordinates of the world $[X\ Y\ Z]$ and the corresponding image points $[x\ y]$. Equation (1), which considers a pinhole camera model [19], can be written as:

$$w\left[x\ y\ 1\right]^T = \boldsymbol{K}\left[\boldsymbol{R}\ t\right]\left[X\ Y\ Z\ 1\right]^T, \tag{1}$$

where w is the arbitrary scale factor, $\boldsymbol{R}$ is the matrix representing the 3D rotation of the camera, t is the translation relative to the world coordinate system, and $\boldsymbol{K}$ is the intrinsic matrix of the camera [18].

Since the pinhole camera does not contain a lens, it does not include the distortion effect. For a better representation of the real camera, it is necessary to include the effect of distortion. This effect can be modeled using radial and tangential distortions. Radial distortion is caused by the spherical shape of the lens, whereas tangential distortion is caused by the decentering and non-orthogonality of the lens components with respect to the optical axis [20]. In the case of modeling radial distortion, only two coefficients were considered in the *EstimateCameraParameters* calibration, which is sufficient for cases where a large distortion is not assumed [21].

The procedure to determine the matrix $\boldsymbol{K}$ is described, for example, in reference [22]. For the determination of $\boldsymbol{K}$, a total of 21 photos containing the calibration checkerboard were taken before the experiment started. One of these photographs can be seen in Fig. 5. After taking the photograph, the mobile phone was untouched and remained in the same place for all the experimental measurements presented in this paper. The result of the *EstimateCameraParameters* functionality is a MATLAB [23] file containing all the necessary parameters for further work with the video.

3.2 Obtaining the coordinates of tracked objects

Video records of all experimental measurements were uploaded from the mobile phone to the computer. For the subsequent work and script creation, MATLAB software [23] was used. After the video was imported into the software, the video was decomposed into frames, which were then analyzed by the algorithm described in Section 3.2. Each frame required modifications to remove the effect of lens distortion. To do this, the *undistortImage* [24] function was used, which uses the intrinsic matrix. The determination of this matrix is described in Section 3.1.

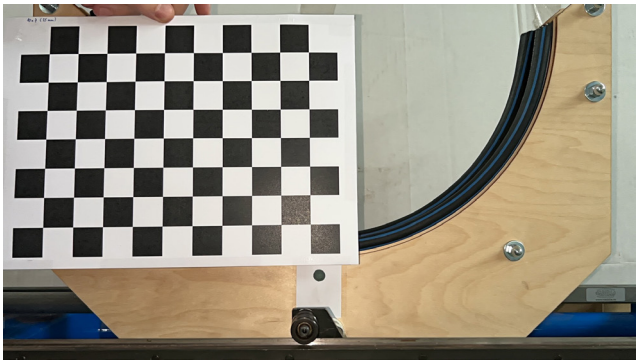

Fig. 5 One of the photos used to obtain the camera parameters

In the next step, four monitoring areas were created in the undistorted frame. These selected areas have been isolated from the frame and further analyzed individually. These areas will henceforth be referred to as windows to distinguish them from the frames. Each window was created manually in the first step of the algorithm, so it contains a tracked object. Thus, one window is created for the ball and three for the reference points. The main reason for their creation is to allow better tracking of individual points and to reduce the background that needs to be removed.

Separation of the tracked object from the background is performed based on colour differentiation. To ensure sufficient colour contrast, several preparatory measures were implemented during the experiments. High-contrast reference points were created using black markers on a white background, and a uniform, single-color background was placed behind the experimental setup to facilitate reliable detection of the ball in MATLAB.

Within the processing algorithm, the colour of each tracked object is selected directly from the first video frame and is assumed to remain constant throughout the recording. In practice, however, the surface of the object rarely exhibits a perfectly uniform colour due to variations in illumination, reflections, and shadows. To account for these effects, an admissible colour tolerance is introduced around the selected reference colour. The magnitude of this tolerance may vary between experiments depending on the prevailing lighting conditions.

Application of the colour filter results in a binary image composed of black and white pixels. White pixels correspond to regions whose colour falls within the specified tolerance of the reference colour and thus represents the tracked object, while black pixels denote the background. An example of the resulting binary images and the effect of the applied filter is shown in Fig. 6.

To identify the center of the tracked objects, a circular Hough transform was applied in each of the filter-adjusted windows. This is a method that can identify the center of a circular cluster in an image at the base of a given radius [25]. The principle of this method can be described using Fig. 7. For each point on an edge, a circle of known radius is created. By drawing such circles, we form an accumulator space, where the intensity at each point expresses how many circles pass through them. The point with the maximum overlap corresponds to the center of the original circle that was detected [26]. In MATLAB, the circular Hough transform can be used using the function *imfindcircles* [27]. The most important parameter is the radius of the circle.

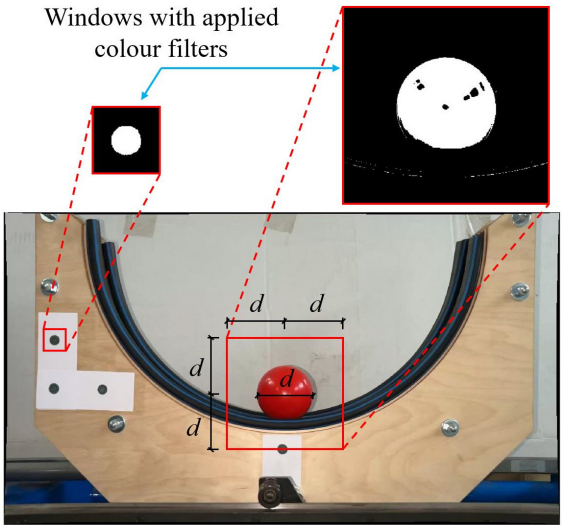

Fig. 6 Example of a video frame showing the creation of only two windows (for a ball and one reference point) with a color filter already applied. Fig. 6 also marks the diameter d of the object being tracked, which is used to adjust the size of the windows.

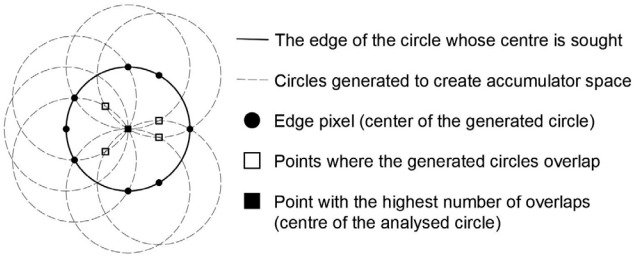

Fig. 7 Illustration to explain the principle of circular Hough transform (inspired by [25])

For each tracked object, this value is determined based on the measurements made in the first frame of the video.

Once the center of the tracked object is successfully identified, the region of interest (ROI) is updated. The window boundaries are adjusted to a distance equal to the object diameter, defined as twice the radius obtained from the circular Hough transform (see Fig. 6). The subsequent video frame is then processed using this updated window position.

Because the video is recorded at a sufficiently high sampling (frame) rate, the displacement of the object between consecutive frames is assumed to be small. Under this assumption, the object remains fully visible within the ROI in the following frame. After the object center is detected in the new frame, the window is repositioned again to maintain the same diameter-based boundary around the object. This procedure is repeated iteratively until the end of the video sequence.

As a result, the algorithm provides the position of the tracked object in each video frame. Knowing the frame rate of the recording allows the time interval between frames to be determined, enabling reconstruction of the object trajectory as a function of time. At this stage, however, all displacement data are still expressed in pixels.

3.3 Post-processing of the data

The result of Section 3.2 is the position of the tracked objects in the video frames. Therefore, it is necessary to carry out the postprocessing of the measured data for a better representation of the results. It is also necessary to convert the results from the video to the realm, which means converting the values of the response from pixels to millimeters.

The primary objective of the analysis is to obtain the dynamic response of the ball absorber, with particular focus on the time evolution of the oscillation amplitude. To this end, it is necessary first to determine the equilibrium position of the ball, corresponding to a state with no motion. An image of the sphere at rest, together with the defined Cartesian coordinate system, is shown in Fig. 8.

The equilibrium position is defined so that both coordinates are equal to zero. The displacement of the ball is then evaluated as the difference between its instantaneous position and the equilibrium position. The displacements in the horizontal and vertical directions are given by:

$$x_{disp,pix,i} = x_i - x_{\text{rest}}\,, \tag{2}$$

$$y_{disp,pix,i} = y_i - y_{\text{rest}}\,, \tag{3}$$

where x_i and y_i denote the coordinates of the ball center in the i-th video frame, x_{rest} and y_{rest} represent the coordinates of the equilibrium position, and $x_{disp,pix,i}$ and $y_{disp,pix,i}$ are the corresponding displacements expressed in pixel units.

In the case of free oscillations, the motion is initiated by displacing the ball from its equilibrium position, and the subsequent relaxation toward rest is recorded. Therefore, the equilibrium position is determined as the average position obtained from the final five video frames. This averaging procedure reduces the influence of random detection errors and provides a robust estimate of the rest position.

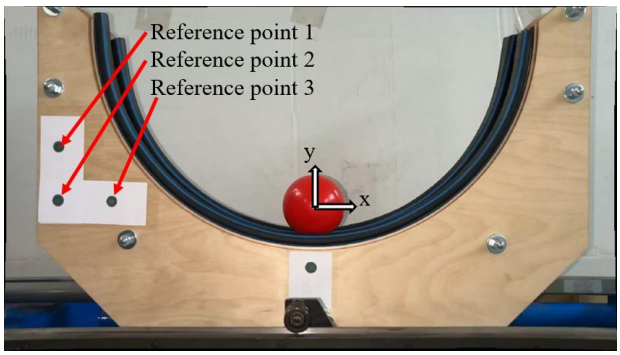

Fig. 8 Video frame shows the ball at rest position. Fig. 8 also contains the numbering of the reference points and displays the coordinate system.

The conversion from pixel units to millimetres is performed using reference points with a known mutual distance. These reference points are created using a 3D-printed template, ensuring a precisely defined spacing. Their positions in each video frame are obtained from the output of the tracking algorithm described in Section 3.2.

Based on the known physical distance between the reference points and their corresponding distance measured in pixels, a spatial calibration factor is determined. This factor represents the physical length of a single pixel in the plane of the reference points. By multiplying the pixel displacements $x_{disp,pix,i}$ and $y_{disp,pix,i}$ given by Eq. (2) and Eq. (3) by this calibration factor, the corresponding displacements of the ball centre are obtained in millimetres. The conversion can be expressed as follows:

$$x_{disp,i} = x_{disp,pix,i} \cdot \frac{x_{\text{points}}}{x_{3,i} - x_{2,i}}, \tag{4}$$

$$y_{disp,i} = y_{disp,pix,i} \cdot \frac{y_{\text{points}}}{y_{1,i} - y_{2,i}}, \tag{5}$$

where x_{points} and y_{points} are the known distances of the reference points in the x and y directions, which are equal to 50 millimeters in the experiment. The variables $x_{2,i}$ and $x_{3,i}$ in Eq. (4) represent the position of the second and third reference points in the i-th frame in the x direction. The positions of the first reference point $y_{1,i}$ and the second reference point $y_{2,i}$ in the y direction are used in Eq. (5). The numbering of the reference points can be seen in Fig. 8. The results in Eqs. (4) and (5) are the displacements of the centre of the ball $x_{disp,i}$ and $y_{disp,i}$ from the i-th frame, in the x and y directions, respectively. These values are already expressed in millimeters.

By converting the position of the ball centre from pixels to millimeters, we obtain the displacement of the ball centre over time, $x_{disp}(t)$ and $y_{disp}(t)$. The system has always been of a single degree of freedom since only the motion of one point is tracked. Representing the displacement in Cartesian coordinates describes the motion along two directions. Since motion occurs along a circular trajectory, the next logical step is to convert the two-dimensional displacement into a physics-aligned angular displacement $\varphi_{disp}(t)$. This representation naturally reflects the underlying dynamics and facilitates further analysis and comparison with numerical simulations.

For these reasons, the subsequent step involves fitting a circle to the measured points and deriving the angular displacement $\varphi_{disp}(t)$ relative to the estimated centre of the trajectory. This procedure also provides metrics that quantitatively assess the quality of the recorded geometry, such as the mean radial deviation from the fitted circle.

The circle fitting itself is performed by solving an overdetermined system of linear equations derived from the general equation of a circle:

$$\left(x_{disp} - x_f\right)^2 + \left(y_{disp} - y_f\right)^2 = \rho_{\text{fit}}^2, \tag{6}$$

where x_f and y_f are the estimates of the circle centre and ρ_{fit} is its radius. By expanding and rearranging the terms, Eq. (6) can be rewritten in linear form:

$$-2x_{disp,i}x_f - 2y_{disp,i}y_f + f = -\left(x_{disp,i}^2 + y_{disp,i}^2\right), \tag{7}$$

where the parameter f in Eq. (7) is defined as:

$$f = x_f^2 + y_f^2 - \rho_{\text{fit}}^2. \tag{8}$$

For the N measured coordinates ($x_{disp,i}$, $y_{disp,i}$), the left-hand side of Eq. (7) can be expressed in matrix form as:

$$\boldsymbol{A} = \begin{pmatrix} -2x_{disp,1} & -2y_{disp,1} & 1 \\ -2x_{disp,2} & -2y_{disp,2} & 1 \\ \vdots & \vdots & \vdots \\ -2x_{disp,N} & -2x_{disp,N} & 1 \end{pmatrix}, \tag{9}$$

and the right-hand side vector is defined as:

$$\boldsymbol{b} = -\begin{pmatrix} x_{disp,1}^2 + y_{disp,1}^2 \\ x_{disp,2}^2 + y_{disp,2}^2 \\ \vdots \\ x_{disp,N}^2 + y_{disp,N}^2 \end{pmatrix}. \tag{10}$$

The parameters of the desired circle are then obtained by solving the system:

$$\boldsymbol{A} \cdot \boldsymbol{p} = \boldsymbol{B}, \tag{11}$$

in the least-squares sense, where:

$$\boldsymbol{p} = \begin{pmatrix} x_f & y_f & f \end{pmatrix}^T. \tag{12}$$

The solution of the system of equations in Eq. (11) is performed using the built-in MATLAB function "*mldivide*" [28]. From the computed vector in Eq. (12), the radius of the desired circle ρ_{fit} can be determined using the rearranged form of Eq. (8) as follows:

$$\rho_{\text{fit}} = \sqrt{x_f^2 + y_f^2 - c}. \tag{13}$$

Based on the geometry of the trajectory determined in this way, the instantaneous distance of the ball centre from the centre of the fitted circle, r_i, is calculated for each time point. This distance is used to evaluate the radial deviation

of the trajectory from the ideal circular path and to quantitatively assess the quality of the fit. The calculation is given by Eq. (14):

$$r_i = \sqrt{\left(x_{disp,i} - x_f\right)^2 + \left(y_{disp,i} - y_f\right)^2} \,. \tag{14}$$

The radial deviation $\varepsilon_{\mathrm{fit},i}$ from the ideal circle is defined as:

$$\varepsilon_{\mathrm{fit},i} = \left| r_i - \rho_{\mathrm{fit}} \right| . \tag{15}$$

From the $\varepsilon_{\mathrm{fit},i}$, statistical measures of the fit quality are determined, namely the root mean square error (RMSE) and the mean absolute error (MAE), which provide quantitative information on the extent of geometric distortion of the trajectory.

Once the centre of the circle has been determined, the angular position of the ball centre is defined using its relative coordinates in the x and y directions, $\Delta x_{disp,i}$ and $\Delta y_{disp,i}$:

$$\Delta x_{disp,i} = x_{disp,i} - x_f \,,\; \Delta y_{disp,i} = y_{disp,i} - y_f \,. \tag{16}$$

The angular displacement $\varphi_{disp,i}$ is then calculated as:

$$\varphi_{disp,i} = \mathrm{atan2}\left(\Delta x_{disp,i}, \Delta y_{disp,i}\right) \tag{17}$$

where "*atan2*" is a built-in MATLAB function for the four-quadrant inverse tangent [29]. It was utilized because it allows the angular displacement of the ball centre relative to the circle centre to be determined unambiguously in all quadrants while correctly preserving its sign. The resulting angular displacement is further processed using the MATLAB function "*unwrap*" [30]. This function removes artificial jumps by multiples of that occur when the angle crosses the $-\pi$ to π boundaries of the "*atan2*" function domain, ensuring a continuous time course of angular displacement corresponding to the smooth motion of the system.

Finally, the angular displacement is smoothed using a one-dimensional median filter with a window size of seven samples. This filter is applied using the "*medfilt1*" function [31], which is a built-in MATLAB function. The reason for applying the filter is to suppress isolated outliers and short-term fluctuations caused by noise during tracking or occasional incorrect detection of the centre of the ball, while preserving the overall shape of the signal and the position of its extremes. The result is a smoother angular deviation curve, which is better suited for subsequent analysis of oscillatory motion. In Section 4 and 5, this modified response will be denoted as φ_{exp} to emphasize that it is the result of an experimental measurement.

4 Tracking algorithm applied to free oscillation data

Section 4 presents the results of the measurements performed using the experimental setup described in Section 2. In all experiments, a sphere with a mass of 0.219 kg and a diameter of 61.5 mm was used. To enhance the performance of the color-based tracking algorithm, a red-colored sphere was selected. The rolling path surface consisted of pipes with an ethylene propylene diene monomer (EPDM) rubber sheath. The pipes had an inner diameter of 6 mm and an outer diameter of 13 mm. The application of these pipes modified the radius of curvature of the rolling path. For the purposes of this study, the spacing between the glued wooden plates was set to 40 mm.

The first results concern the position of the ball centre recorded along the x and y axes. Fig. 9 and Fig. 10 show the ball centre positions obtained after applying Eq. (4) and Eq. (5) to the experimental data. These results represent the displacements converted from pixel coordinates to millimeters. Specifically, Fig. 9 illustrates the time evolution of the displacement $x_{disp}(t)$, while Fig. 10 presents the corresponding time evolution of $y_{disp}(t)$.

When examining the displacement results in the y direction shown in Fig. 10, minor inaccuracies can be observed. These manifest as occasional negative displacement values, which would imply that the position y_{disp} is lower than the reference rest position y_{rest} (see Eq. (3)). The largest

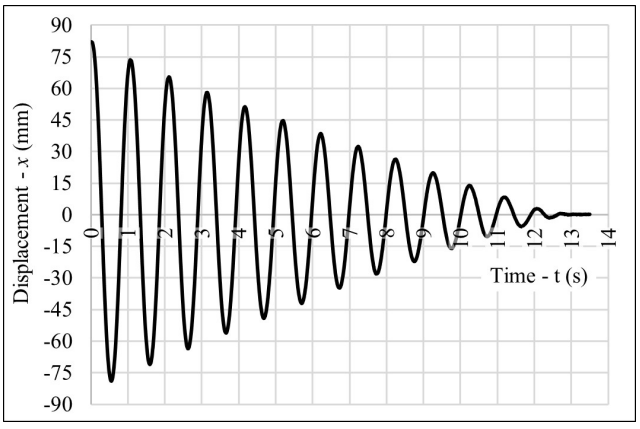

Fig. 9 Time history of the horizontal displacement x_{disp} of the ball centre

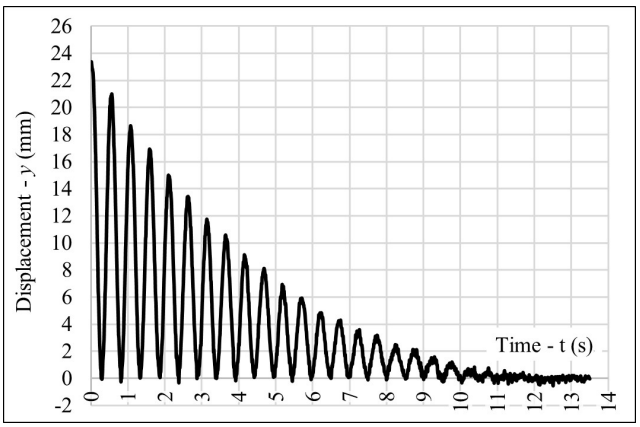

Fig. 10 Time history of the vertical displacement y_{disp} of the ball centre

deviation occurs between 2 and 3 s, reaching −0.319 mm. These deviations are most likely caused by small errors in the detection of the ball centre or by inaccuracies in the determination of the reference position y_{rest}. Importantly, these local inconsistencies do not influence the subsequent analysis, as they are naturally mitigated when the two-dimensional displacement is converted into angular coordinates.

By fitting a circle to the experimental data, the results summarized in Table 1 were obtained. The circle that best matches the measured trajectory has a fitted radius ρ_{fit} equal to 164.381 mm. The quality of the fit is confirmed by the low values of the root mean square error (RMSE = 0.197 mm) and the mean absolute error (MAE = 0.155 mm), indicating only a very small deviation of the measured data from the fitted circular trajectory.

The radial deviation ε_{fit} is shown in Fig. 11. A closer inspection reveals two pronounced local maxima with values of 0.805 mm and 0.787 mm. The distribution of the radial deviation values is further illustrated by the histogram in Fig. 12, which shows the number of occurrences within bins of width 0.1 mm. It is evident that the largest proportion of deviations lies within the interval from 0 to 0.1 mm. By summing the data points within the range of 0 to 0.4 mm, a total of 1530 samples are obtained, which corresponds to approximately 94.39 % of the total 1621 data points. This indicates that nearly 94.39 % of the measured trajectory exhibits a radial deviation smaller than 0.4 mm, confirming the high geometric consistency of the recorded motion with an ideal circular path.

Fig. 13 shows the angular displacement φ_{exp}. In this experiment, the initial angular deflection was 31.46°. The observed response corresponds to free damped oscillation, with the motion gradually decaying until the ball comes to rest at approximately 13 s.

Table 1 Circle fitting results for the experimental trajectory

	ρ_{fit} (mm)	RMSE (mm)	MAE (mm)
Spacing 40	164.381	0.197	0.155

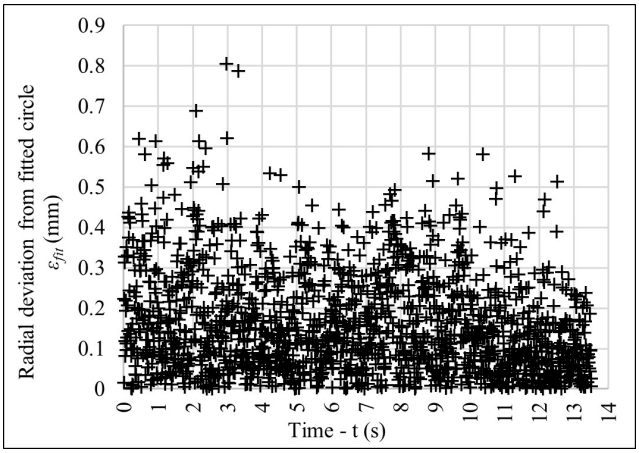

Fig 11 Radial deviation ε_{fit} of the measured trajectory from the fitted circle

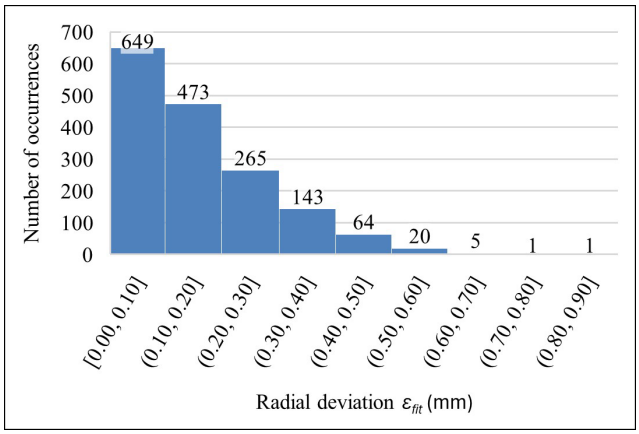

Fig 12 Histogram of radial deviations ε_{fit} showing the distribution of deviations within 0.1 mm bins. The numbers above the bars in the graph show the exact number of occurrences.

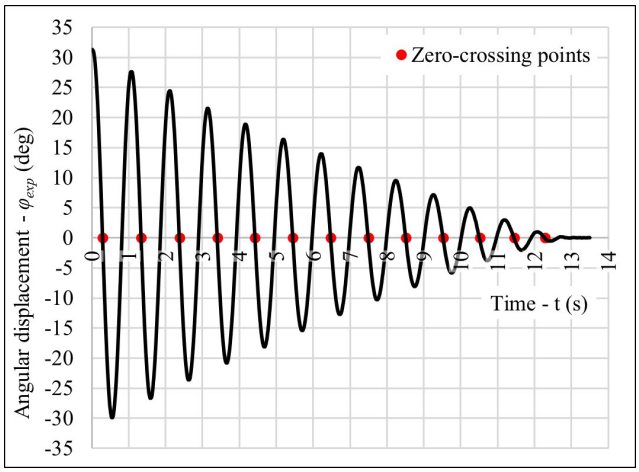

Fig. 13 Angular displacement φ_{exp} of the ball centre: Zero-crossing points used for the determination of individual oscillation periods are indicated by red dots

A more detailed insight into the oscillatory behavior is obtained by analyzing the evolution of the oscillation period over time. From the measured full periods, a gradual decrease in the cycle duration with decreasing amplitude can be observed. At the beginning of the motion, the periods are approximately 1.04 s, decreasing to about 1.02–1.03 s in the mid-range of the oscillation, and further shortening to approximately 0.83 s toward the end of the motion. The trend is relatively smooth, with a slightly accelerated decrease in the period during the final cycles. For clarity, the individual oscillation periods are plotted as a function of their index in Fig. 14, where the index corresponds to the sequential order of each measured oscillation period.

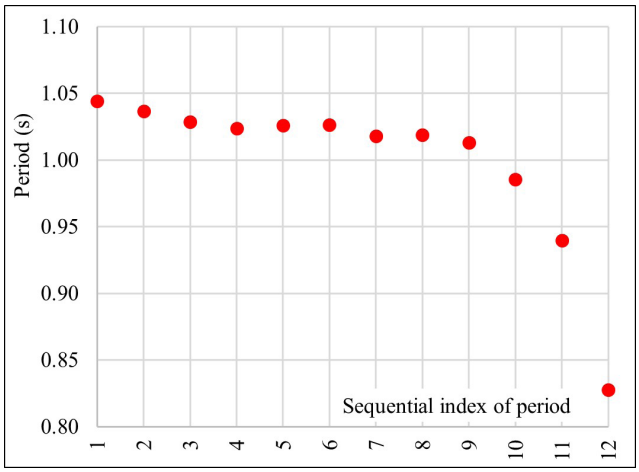

Fig 14 Measured oscillation periods plotted as a function of their sequential index

5 Numerical solution and experimental data fitting

Section 5 focuses on the numerical solution of the analytical governing equations, which is employed to fit the experimentally obtained data. The numerical model is calibrated by adjusting the damping parameters so that the simulated system response matches the experimental measurements. Energy dissipation is represented through a combination of viscous damping and rolling friction described by Coulomb's law (see, e.g., [32]).

5.1 Derivation of the governing equations

Due to the nature of the system, the absorber motion is confined to a single plane. The rolling motion of the ball is described by the angular displacement φ_{sim}, with time derivatives. For brevity, the explicit time dependence is omitted in the following derivation. The time-independent parameters of the system are the ball mass m, ball radius r, curvature radius of the rolling path R, radius of the rolling pipes r_p, and the axial distance between the pipe centres s_p. The pipe centres are assumed to be located above the centre line of the last wooden plate of thickness 2 mm, therefore s_p = spacing + 2 mm. The gravitational acceleration is denoted by g. The system geometry is illustrated in Fig. 15.

From the geometry, two kinematic constraints follow. First, continuous contact between the ball and the supporting pipes is assumed, without separation or penetration. Under this assumption, the centre of the ball moves along a circular trajectory of radius:

$$\rho = R_c - r - y_p\,, \tag{18}$$

with y_p is the vertical distance between the centre of the ball and the centres of the pipes, given by:

$$y_p = \sqrt{\left(r + r_p\right)^2 - \left(0.5 s_p\right)^2}\,. \tag{19}$$

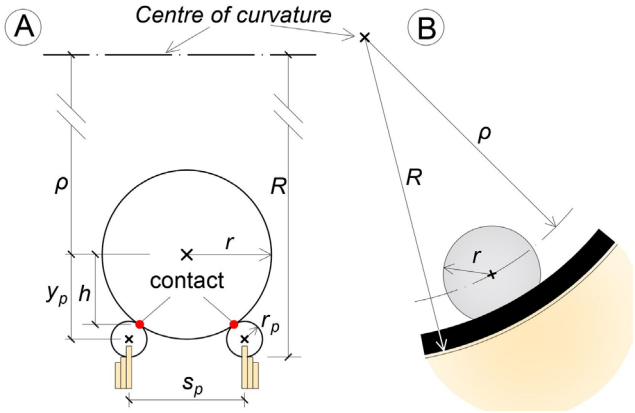

Fig. 15 Schematic illustration of the system geometry: A - view along the direction of ball motion; B - side view of the geometry

Second, pure rolling without slipping is assumed, leading to the kinematic relation:

$$\omega = \frac{\rho}{r}\dot{\varphi}_{sim}\,, \tag{20}$$

where ω is the spin angular velocity of the ball about its own centre and $\dot{\varphi}_{sim}$ is the angular velocity of the orbital motion of the ball centre along the curved path.

With reference to Fig. 15, the horizontal and vertical displacements of the ball centre are expressed as:

$$x(t) = \rho \sin\varphi_{sim}, \quad y(t) = \rho\cos\varphi_{sim}\,. \tag{21}$$

Differentiation of Eq. (21) yields to:

$$\dot{x} = \rho\cos\varphi_{sim}\,\dot{\varphi}_{sim}, \quad \dot{y} = -\rho\sin\varphi_{sim}\,\dot{\varphi}_{sim}\,. \tag{22}$$

The total kinetic energy consists of translational and rotational contributions. Using Eq. (22) and the rolling constraint Eq. (20), it can be written as:

$$\begin{aligned} T &= \frac{1}{2}m\left(\dot{x}^2 + \dot{y}^2\right) + \frac{1}{2}J\omega^2 = \\ &= \frac{1}{2}m\left(\rho^2\dot{\varphi}_{sim}^2\right) + \frac{1}{2}J\left(\frac{\rho^2}{r^2}\dot{\varphi}_{sim}^2\right), \end{aligned} \tag{23}$$

where $J = (2/5)mr^2$ is the moment of inertia of the solid sphere. The gravitational potential energy is given by:

$$V = mg\rho\left(1 - \cos\varphi\right). \tag{24}$$

The model incorporates two non-conservative moments representing energy dissipation: viscous damping along the rolling path and rolling resistance. This combined dissipation model is motivated by experimental observations reported in, e.g., [33]. If required, either contribution can be omitted.

The viscous damping moment is expressed as:

$$M_\varphi = \rho\, c_{vis}\,\dot{\varphi}_{sim}\,, \tag{25}$$

with c_{vis} is the viscous damping coefficient. The rolling damping moment is described using a regularized Coulomb friction model,

$$M_{rr} = c_{rr}\, N\, h \frac{\dot{\varphi}_{sim}}{\sqrt{\dot{\varphi}_{sim}^2 + \varepsilon_{sing}{}^2}}, \tag{26}$$

where c_{rr} is the rolling resistance coefficient, N is the normal force, h is the vertical distance between the ball center and the contact point with the pipes, and ε_{sing} is a small regularization parameter introduced to ensure numerical stability near zero angular velocity. This formulation ensures that the rolling damping moment always acts against the instantaneous direction of motion.

The normal force N in Eq. (26) is approximated as:

$$N \approx mg\cos\varphi_{sim} + m\rho\dot{\varphi}_{sim}^2. \tag{27}$$

In Eq.(27) the first term represents the gravitational contribution projected onto the radial direction and the second term accounts for the centripetal effect associated with the circular motion of the ball centre. The geometric distance h follows as

$$h = \frac{r}{r + r_p} \cdot y_p. \tag{28}$$

Using the expressions for the kinetic and potential energies together with the damping moments, the equation of motion governing the free oscillation of the rolling ball is obtained from the second-order Lagrange equation in the form:

$$\begin{aligned} &m\rho^2\left(1 + \frac{J}{mr^2}\right)\ddot{\varphi}_{sim} + mg\rho\sin\left(\varphi_{sim}\right) \\ &+\rho\, c_{vis}\,\dot{\varphi}_{sim} + c_{rr}\, N\, h \frac{\dot{\varphi}_{sim}}{\sqrt{\dot{\varphi}_{sim}^2 + \varepsilon_{sing}{}^2}} = 0. \end{aligned} \tag{29}$$

To enable a consistent interpretation of the damping parameter within the chosen single-degree-of-freedom (SDOF) formulation in the angular coordinate, the equation of motion is linearized. The rolling resistance term is neglected, and the small-angle approximation $\sin(\varphi_{sim}) \approx \varphi_{sim}$ is applied. This yields a linear viscously damped oscillator of the form:

$$m\rho^2\left(1 | \frac{J}{mr^2}\right)\ddot{\varphi} + \rho\, c_{vis}\,\dot{\varphi} + mg\rho\varphi = 0. \tag{30}$$

Dividing Eq. (30) by ρ and assuming an exponential solution $\varphi(t) = e^{\lambda t}$, the characteristic equation becomes:

$$m\rho\left(1 | \frac{J}{mr^2}\right)\lambda^2 + c_{vis}\lambda + mg = 0. \tag{31}$$

Critical viscous damping corresponds to a double root of Eq. (31), yielding:

$$c_{vis,crit} = 2\sqrt{m^2\rho\left(1 | \frac{J}{mr^2}\right)g} = 2m\sqrt{g\rho\left(1 | \frac{J}{mr^2}\right)}. \tag{32}$$

The dimensionless viscous damping ratio is then defined as:

$$\zeta = \frac{c_{vis}}{c_{vis,crit}} = \frac{c_{vis}}{2m\sqrt{g\rho\left(1 | \frac{J}{mr^2}\right)}}. \tag{33}$$

This formulation allows the viscous damping coefficient c_{vis} to be expressed in terms of the critical damping of the linearized SDOF system as a dimensionless damping ratio ζ.

5.2 Damping parameter identification via numerical fitting

Section 5.2 describes the procedure used to identify suitable damping parameters such that their combined effect reproduces the experimentally observed decay of oscillation amplitude. The objective is to determine the viscous damping coefficient c_{vis} and the rolling resistance coefficient c_{rr} by fitting the numerical response of the model to experimental data.

For clarity, all parameters of the absorber used in the numerical simulations are summarized in Table 2. These parameters correspond to those employed in the experimental measurements, including the geometry of the setup. It should be noted that the curvature radius R_c does not equal 200 mm, which would correspond to the upper edge of the track. Instead, a value of 204 mm is used, representing the level of the first contact point from above, where the pipe of radius r_p is placed. The quantities ρ and h are calculated according to Eq. (18) and Eq. (28), respectively, and are listed to provide additional context for the numerical model. Using the parameters given in Table 2, the critical viscous damping of the absorber was evaluated according to Eq. (32), resulting in $c_{vis,crit} = 0.663$.

It is also necessary to emphasize the difference between ρ_{fit} and ρ. Value of ρ_{fit} was obtained by fitting a circle to the experimental data and may contain distortions, therefore ρ for numerical simulations were taken directly from the geometry of the experimental setup.

Prior to the fitting procedure, all oscillation amplitudes are extracted from the experimental angular displacement response. To avoid detecting spurious peaks in regions dominated by noise, only peaks exceeding 1% of the absolute value of the first amplitude are considered. This criterion ensures that the analysis focuses on physically meaningful oscillations.

The numerical solution of the equation of motion is obtained in MATLAB using the function "*ode45*" [34].

Table 2 Absorber parameters for numerical simulations

r (mm)	m (kg)	r_p (mm)	S_p (mm)	R_c (mm)	ρ (mm)	h (mm)
30.75	0.219	6.5	42	204	166.733	25.398

For the fitting process, particular attention is paid to the selection of initial conditions. During the experiment, the sphere was placed manually onto the track, and considerable effort was made to avoid imparting any initial velocity. Nevertheless, to reduce uncertainty associated with the initial conditions, the numerical simulation is initialized at the first amplitude following a crossing of the equilibrium position. At this point, the angular displacement is known, and the angular velocity is zero. Although this does not correspond to the physical start of motion in the experiment, it is consistently treated as $t = 0$ s in the simulation.

In analogy with the experimental data processing, all oscillation amplitudes are also identified from the simulated angular displacement. The detected amplitudes are then paired exclusively according to their order: the first simulated peak is matched with the first experimental peak, the second with the second, and so on. The total number of paired amplitudes n_A is defined as the minimum of the number of experimental or as the minimum of simulated peaks.

The quality of the fit is evaluated using a least-squares optimization criterion, hereafter referred to as the cost function Q, defined as:

$$Q\left(c_{vis}, c_{rr}\right) = \sum_{j=1}^{n_A} \left[A_{sim,j}\left(c_{vis}, c_{rr}\right) - A_{exp,j} \right]^2, \tag{34}$$

where $A_{sim,i}(c_{vis}, c_{rr})$ are the absolute amplitudes of the simulated angular displacement φ_{sim} obtained from the simulation for a given set of damping parameters, and $A_{exp,i}$ are the corresponding amplitudes of the experimentally measured angular displacement φ_{exp}.

The optimal values of c_{vis} and c_{rr} are identified by minimizing $Q(c_{vis}, c_{rr})$ using the MATLAB optimization routine "*fmincon*" [35]. The initial estimates are chosen as $c_{vis} = 0.1$ and $c_{rr} = 0.1$. The optimization is terminated when convergence is achieved, defined either by a negligible reduction of the cost function between successive iterations, a vanishing sensitivity of the cost function to parameter variations, or when a predefined maximum number of function evaluations is reached.

For additional quantitative assessment of the fit quality, the root mean square (RMS) value can be evaluated from the cost function as:

$$\mathrm{RMS} = \sqrt{\frac{Q}{n_A}}\,. \tag{35}$$

It should be emphasized that the optimization is performed exclusively by minimizing the cost function Q. The RMS value is evaluated a posteriori and serves only as a descriptive measure of the fit quality.

The identified damping parameters therefore provide a physically interpretable description of the energy dissipation mechanisms governing the observed decay of the oscillation amplitude.

5.3 Results

The parameter identification procedure described in Section 5.2 yields a unique set of damping parameters that provides the best agreement between the numerical simulation and the experimental data. The identified values of the viscous damping coefficient c_{vis} and the rolling resistance coefficient c_{rr} are summarized in Table 3, together with the corresponding quantitative measures of the fit quality. In addition, the viscous damping is expressed in terms of the dimensionless damping ratio ζ, defined relative to the critical damping of the linearized SDOF system. The damping ratio is evaluated according to Eq. (33), using the critical damping value $c_{vis,crit} = 0.663$.

The value of the cost function at the optimum is $Q = 0.002305$ rad^2, which corresponds to 7.568 deg^2. From this value, the root mean square (RMS) error of the matched amplitudes is obtained as 0.010 rad (i.e., 0.574 deg). When related to the first oscillation amplitude used as the initial condition of the simulation, $\varphi_0 = -29.96$ deg, the RMS error corresponds to approximately 1.9%. In total, $n_A = 23$ pairs of experimental and simulated amplitudes were included in the evaluation.

A direct comparison of the angular displacement time histories obtained from the experiment and the numerical simulation is shown in Fig. 16. The grey dashed curve denotes the initial and final segments of the experimental signal that were excluded from the optimization, as discussed in Section 5.2. The black solid curve represents the experimental data used for parameter identification, while the red curve corresponds to the simulated response computed using the identified damping parameters. The time axis refers to the original experimental record. The numerical simulation starts at $t = 0.56$ s with the initial angular displacement set equal to the experimentally measured amplitude at the first peak following the passage through the equilibrium position.

The comparison reveals a very good agreement between the simulation and the experiment over the entire fitting

Table 3 Identified damping parameters and RMS error for the experiment with the initial angular displacement $\varphi_0 = -29.96$ deg

c_{vis}	ζ	c_{rr}	Q (rad^2)	Q (deg^2)	RMS (rad)	RMS (deg)
0.1359	0.205	0.2724	0.0023	7.568	0.010	0.574

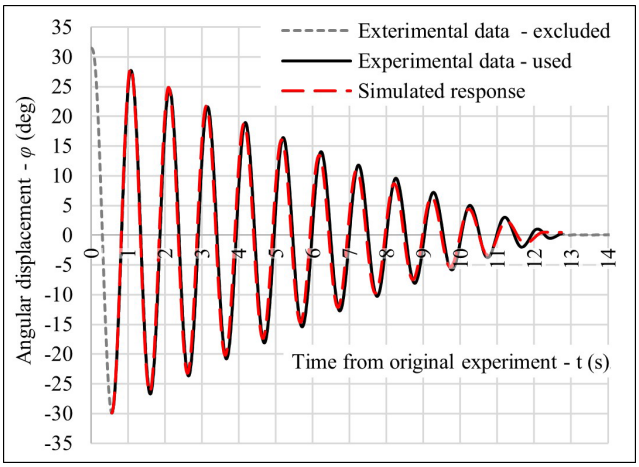

Fig. 16 Comparison of experimental and simulated angular displacement time histories for the experiment with the initial angular displacement $\varphi_0 = -29.96$ deg

interval. Both the phase of oscillation and the decay envelope are reproduced accurately, from the initial large-amplitude oscillations down to the late-stage small displacements. Local discrepancies remain on the order of tenths of a degree and do not affect the overall decay trend. A noticeable difference appears only in the very last part of the record, where the experimental motion still exhibits small oscillations while the simulated response has already settled to rest. This final experimental peak was not included in the optimization because it does not have a corresponding simulated amplitude, which is why only 23 amplitudes were considered.

Fig. 17 presents a comparison of the absolute oscillation amplitudes obtained from the experiment and the simulation. The experimental amplitudes $A_{exp,i}$ and the simulated amplitudes $A_{sim,i}$ lie close to each other and follow a monotonic decay toward zero. This confirms that the identified

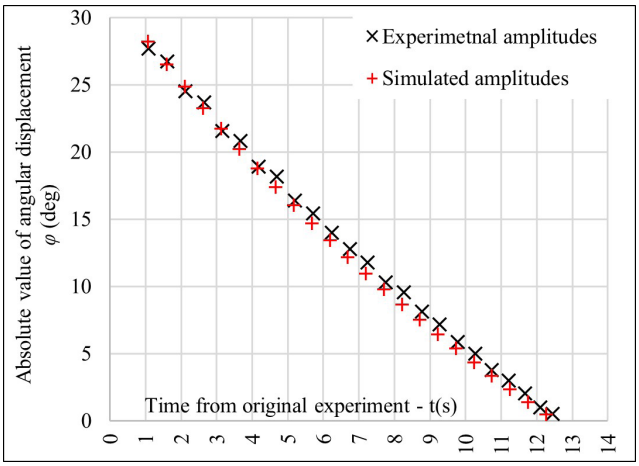

Fig. 17 Comparison of experimental and simulated angular displacement amplitudes for the experiment with the initial angular displacement $\varphi_0 = -29.96$ deg

damping parameters capture the dominant energy dissipation mechanisms governing the amplitude reduction.

The differences between the simulated and experimental amplitudes are shown in Fig. 18 as a function of the amplitude index. The residuals are predominantly negative in the later stages, typically ranging from approximately −0.9 deg to −0.2 deg, indicating a slightly faster decay predicted by the numerical model at low amplitudes. The first few peaks exhibit small positive deviations of up to about 0.5 deg. Overall, the scatter of the residuals remains small and does not exhibit any systematic drift, which further supports the robustness of the identified parameters. The observed tendency toward slightly stronger damping in the simulation at very low velocities may be attributed to the simplified representation of rolling resistance in the vicinity of zero angular speed.

The obtained results indicate that the combined viscous damping and rolling resistance model can reproduce the experimentally observed decay of oscillation amplitudes with good accuracy. The agreement between simulation and experiment is maintained over a wide range of amplitudes, with only minor deviations at very small oscillations.

To further investigate the origin of the deviations between the simulated and experimental amplitudes observed in Fig. 18, the analysis was extended by additional experiments with larger initial angular displacements. The purpose of this extension was to evaluate whether the observed discrepancies are primarily related to the specification of the initial conditions or whether they originate from higher velocities occurring at larger oscillation amplitudes.

In addition to the experiment with the initial angular displacement $\varphi_0 = -29.96$ deg, two further experiments with

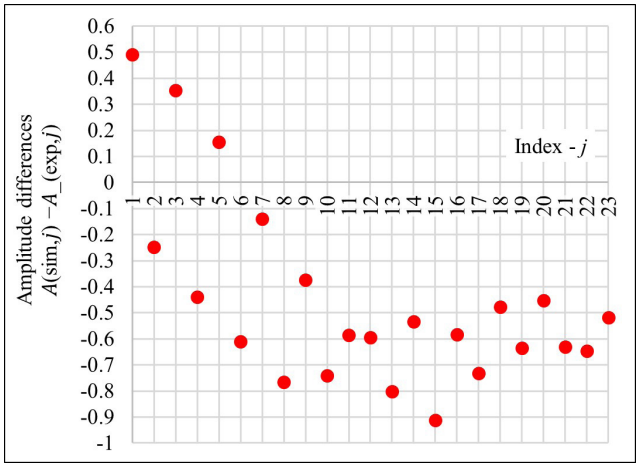

Fig. 18 Difference between simulated and experimental angular displacement amplitudes for the experiment with the initial angular displacement $\varphi_0 = -29.96$ deg: The amplitude differences $A_{sim,i} - A_{exp,i}$ are plotted as a function of the amplitude index j

initial displacements $\varphi_0 = -35.771$ deg and $\varphi_0 = -39.695$ deg were analyzed using the same identification procedure. The inclusion of these additional experiments allows a direct comparison of the model performance under different initial conditions and therefore provides a more robust validation of the proposed numerical model.

For the experiment with the initial angular displacement $\varphi_0 = -35.771$ deg, the comparison of the experimental and simulated angular displacement time histories is shown in Fig. 19. The comparison of the corresponding oscillation amplitudes is presented in Fig. 20, and the differences between the simulated and experimental amplitudes are shown in Fig. 21. The identified damping parameters and the resulting RMS error for this experiment are summarized in Table 4.

The same analysis was subsequently performed for the experiment with the initial angular displacement $\varphi_0 = -39.695$ deg. The comparison of the experimental and simulated angular displacement time histories is presented in Fig. 22, while the corresponding oscillation amplitudes and their differences are shown in Fig. 23 and Fig. 24, respectively. The identified damping parameters and the resulting RMS error are summarized in Table 5.

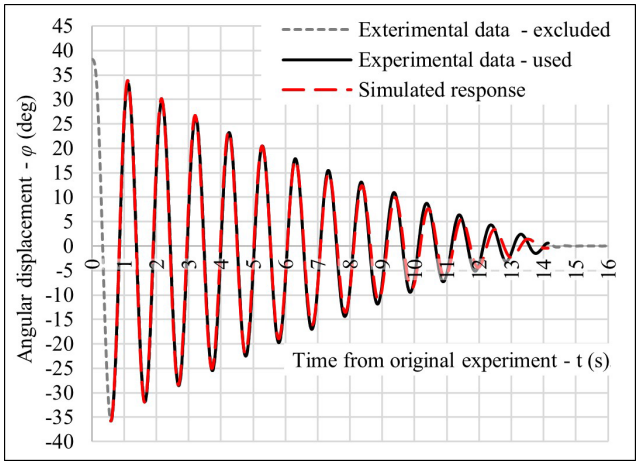

Fig. 19 Comparison of experimental and simulated angular displacement time histories for the experiment with the initial angular displacement $\varphi_0 = -35.771$ deg

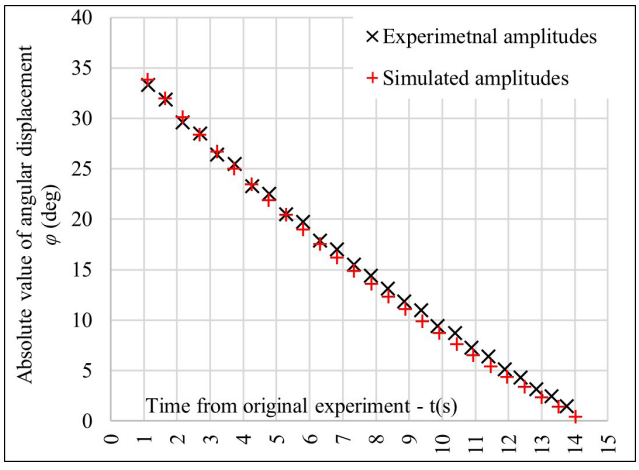

Fig. 20 Comparison of experimental and simulated angular displacement amplitudes for the experiment with the initial angular displacement $\varphi_0 = -35.771$ deg

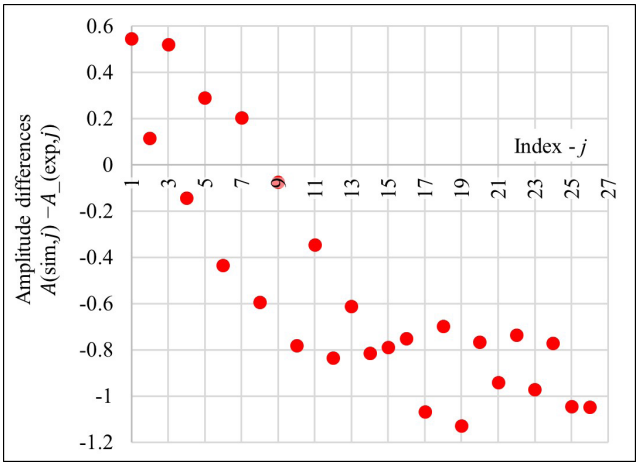

Fig. 21 Difference between simulated and experimental angular displacement amplitudes for the experiment with the initial angular displacement $\varphi_0 = -35.771$ deg: The amplitude differences $A_{sim,i} - A_{exp,i}$ are plotted as a function of the amplitude index j

For clarity, the identified parameters and the corresponding RMS errors for all considered initial conditions are summarized in Table 6.

The comparison of the results obtained for the three different initial displacements shows that the identified damping parameters remain relatively consistent despite the significantly different initial amplitudes. This indicates that the parameter identification procedure is stable and that the

Table 4 Identified damping parameters and RMS error for the experiment with the initial angular displacement $\varphi_0 = -35.771$ deg

c_{vis}	ζ	c_{rr}	Q (rad^2)	Q (deg^2)	RMS (rad)	RMS (deg)
0.1279	0.193	0.2860	0.0041	13.459	0.013	0.765

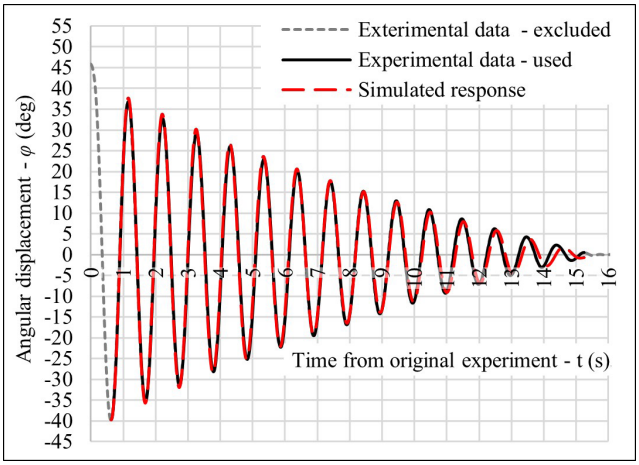

Fig. 22 Comparison of experimental and simulated angular displacement time histories for the experiment with the initial angular displacement $\varphi_0 = -39.695$ deg

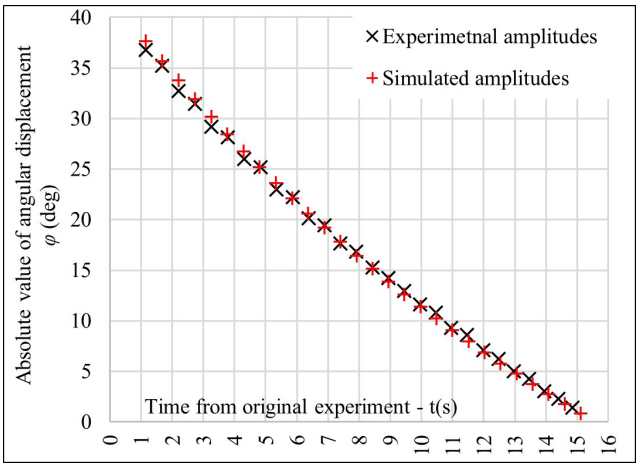

Fig. 23 Comparison of experimental and simulated angular displacement amplitudes for the experiment with the initial angular displacement $\varphi_0 = -39.695$ deg

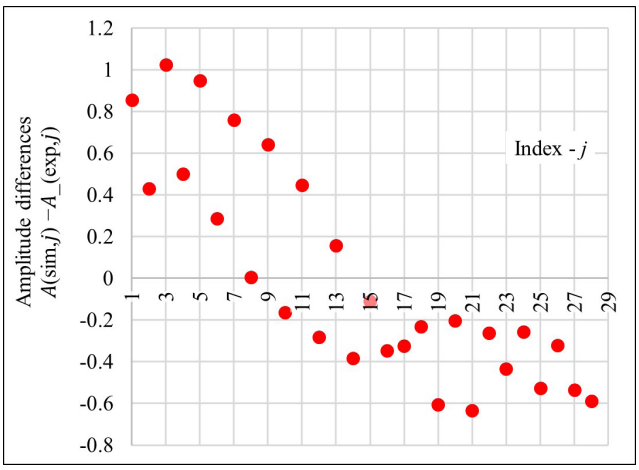

Fig. 24 Difference between simulated and experimental angular displacement amplitudes for the experiment with the initial angular displacement $\varphi_0 = -39.695$ deg: The amplitude differences $A_{sim,i} - A_{exp,i}$ are plotted as a function of the amplitude index j

Table 5 Identified damping parameters and RMS error for the experiment with the initial angular displacement $\varphi_0 = -39.695$ deg

c_{vis}	ζ	c_{rr}	Q (rad^2)	Q (deg^2)	RMS (rad)	RMS (deg)
0.1233	0.186	0.2831	0.0014	4.596	0.007	0.405

Table 6 Comparison of identified damping parameters and RMS errors for different initial angular displacements

φ_0 (deg)	n_a	c_{vis}	ζ	c_{rr}	Q (deg^2)	RMS (deg)
−29.96	23	0.1359	0.205	0.2724	7.568	0.574
−35.771	26	0.1279	0.193	0.2860	13.459	0.765
−39.695	28	0.1233	0.186	0.2831	4.596	0.405

adopted numerical model captures the dominant dissipative mechanisms of the system.

A comparison of the residual amplitude differences (Fig. 18, Fig. 21 and Fig. 24) reveals that a similar pattern of deviations occurs for all analyzed experiments. In each case, the numerical model slightly underestimates the amplitudes of the first oscillation cycles, resulting in small positive differences between the simulated and experimental amplitudes. As the oscillation amplitude decreases, the agreement between the simulation and the measurements gradually improves.

Since this behavior is observed for all tested initial conditions, the deviations cannot be attributed to inaccuracies in the specification of the initial angle. Instead, the results indicate that the discrepancies observed during the first oscillation cycles are more likely to be associated with higher velocities occurring at larger oscillation amplitudes. Under these conditions, the simplified damping representation used in the numerical model may slightly underestimate the energy dissipation present in the physical system. As the oscillation amplitude decreases and the velocities become lower, the agreement between the model and the measurements improves.

Overall, the extended analysis confirms that the identified damping parameters are robust with respect to variations in the initial conditions and that the remaining discrepancies observed in the first oscillation peaks are primarily related to velocity-dependent physical effects rather than to inaccuracies in the prescribed initial displacement.

6 Conclusions

One of the main objectives of this paper was to present an algorithm for the analysis of experimental measurements of a ball absorber response based on video recordings. The algorithm was applied to data obtained from experiments carried out on a specially designed experimental track that constrains the ball motion to a planar trajectory. This constraint is achieved by guiding the rolling motion along a pair of parallel rails, whose mutual spacing can be adjusted, allowing for parametric variation of the track geometry and thus e.g., the rolling frequency, if required.

Free oscillation experiments were conducted on this track and subsequently processed using the proposed video-based analysis algorithm. From the recorded video data, the planar coordinates of the ball motion were extracted and post-processed. By fitting a circle to the measured trajectory, the Cartesian coordinates were transformed into a radial coordinate system, allowing the motion to be described solely in terms of the angular displacement from the equilibrium position. This transformation enabled a compact and physically meaningful description of the absorber dynamics and formed the basis for the subsequent analysis.

In the next stage, the equations of motion describing the ball absorber moving along the rail track were derived. The physical model was constructed to correspond closely to the experimental configuration and incorporated two dissipation mechanisms: viscous damping and rolling resistance described by Coulomb's law. The model parameters were identified through numerical optimization, in which the damping coefficients were adjusted so that the simulated response matched the experimentally observed decay of oscillation amplitudes.

Based on the fitting results, it can be concluded that, in the present case, the combined viscous damping and rolling resistance model provides a realistic and physically interpretable description of the dissipation processes occurring in the experimental system. The combined action of both mechanisms successfully reproduces the experimentally observed decay of oscillation amplitudes over a wide dynamic range. Minor discrepancies between the numerical simulation and the experimental measurements were observed during the first oscillation cycles and at the end of the motion, in the region of very small amplitudes.

Additional validation was performed for several different initial angular displacements in order to evaluate the influence of the initial conditions on the agreement between the numerical model and the experimental measurements. The analysis showed that the identified damping parameters remain consistent across the analysed cases and that the characteristic deviations observed during the first oscillation cycles occur for all tested initial conditions. This behaviour indicates that the discrepancies are not primarily caused by inaccuracies in the prescribed initial displacement but are more likely associated with higher velocities occurring at larger oscillation amplitudes. These findings confirm the robustness of the proposed parameter identification approach.

The remaining deviations are therefore likely related to simplifications adopted in the damping model, which does not account for additional effects such as local deformation of the ball–rail contact or other nonlinear contact phenomena. Incorporating such effects represents a natural direction for future work and may further improve the accuracy of the numerical model, particularly in the low-amplitude regime.

Acknowledgement

The financial support of the grant program financed by the Ministry of Education, Youth and Sports of the Czech Republic through VSB–TUO SGS SP2025/067 and from the budget for the conceptual development of science, research, and innovations is highly acknowledged.

References

[1] Kaláb, Z. "Influence of vibrations on structures", Acta Montanistica Slovaca, 23(3), pp. 293–311, 2018. [online] Available at: https://actamont.tuke.sk/pdf/2018/n3/6kalab.pdf [Accessed: 10 December 2025]

[2] Singh, P. K., Roy, M. P. "Damage to surface structures due to blast vibration", International Journal of Rock Mechanics and Mining Sciences, 47(6), pp. 949–961, 2010. https://doi.org/10.1016/j.ijrmms.2010.06.010

[3] Ruuska, A., Häkkinen, T. "Material Efficiency of Building Construction", Buildings, 4(3), pp. 266–294, 2014. https://doi.org/10.3390/buildings4030266

[4] Kavyashree, B. G., Patil, S., Rao, V. S. "Review on vibration control in tall buildings: from the perspective of devices and applications", International Journal of Dynamics and Control, 9(3), pp. 1316–1331, 2021. https://doi.org/10.1007/s40435-020-00728-6

[5] Chopra, A. K. "Dynamics of Structures: Theory and Applications to Earthquake Engineering", Prentice Hall, 1995. ISBN 9780138552145

[6] Náprstek, J., Fischer, C., Pirner, M., Fischer, O. "Non-linear Model of a Ball Vibration Absorber", In: Papadrakakis, M., Fragiadakis, M., Plevris, V. (eds.) Computational Methods in Earthquake Engineering, Springer, 2013, pp. 381–396. ISBN 9789400765726 https://doi.org/10.1007/978-94-007-6573-3_18

[7] Kawulok, M., Pospisil, S., Freiherrova, N., Juracka, D. "Numerical Simulation of a Planar Model of a Ball Absorber in a Spherical Dish", Periodica Polytechnica Civil Engineering, 67(3), pp. 855–866, 2023. https://doi.org/10.3311/PPci.21725

[8] Kawulok, M., Čermák, M., Pospíšil, S., Juračka, D. "Numerical Procedure for Solving the Nonlinear Behaviour of a Spherical Absorber", Periodica Polytechnica Civil Engineering, 68(4), pp. 1367–1377, 2024. https://doi.org/10.3311/PPci.25903

[9] Sun, L., Li, S., Zhang, F. "Effect of Self-Resetting Ball Absorber on the Mechanical Properties of the Fabricated Structure and Its Influencing Factors: Theory and Experimentation", Journal of Vibration Engineering & Technologies, 10(3), pp. 897–917, 2022. https://doi.org/10.1007/s42417-021-00418-3

[10] Li, J., Zhang, Z., Chen, J. "Experimental Study on Vibration Control of Offshore Wind Turbines Using a Ball Vibration Absorber", Energy and Power Engineering, 4(3), pp. 153–157, 2012. https://doi.org/10.4236/epe.2012.43021

[11] Chen, J., Georgakis, T. C. "Tuned rolling-ball dampers for vibration control in wind turbines", Journal of Sound and Vibration, 332(21), pp. 5271–5282, 2013. https://doi.org/10.1016/j.jsv.2013.05.019

[12] Pirner, M. "Actual behaviour of a ball vibration absorber", Journal of Wind Engineering and Industrial Aerodynamics, 90(8), pp. 987–1005, 2002. https://doi.org/10.1016/S0167-6105(02)00215-5

[13] Matta, E. "Ball vibration absorbers with radially-increasing rolling friction", Mechanical Systems and Signal Processing, 132, pp. 353–379, 2019. https://doi.org/10.1016/j.ymssp.2019.06.033

[14] MathWorks "Computer Vision Toolbox: Design and test computer vision systems", [online] Available at: https://www.mathworks.com/products/computer-vision.html [Accessed: 10 December 2025]

[15] Pospíšil, S., Fischer, C., Náprstek, J. "Experimental analysis of the influence of damping on the resonance behavior of a spherical pendulum", Nonlinear Dynamics, 78, pp. 371–390, 2014. https://doi.org/10.1007/s11071-014-1446-6

[16] Pospíšil, S., Fischer, C., Náprstek, J. "Experimental and theoretical analysis of auto-parametric stability of pendulum with viscous dampers", Acta Technica CSAV (Ceskoslovensk Akademie Ved), 56(4), pp. 359–378, 2011. [online] Available at: https://www.researchgate.net/publication/289007526_Experimental_and_theoretical_analysis_of_auto-parametric_stability_of_pendulum_with_viscous_dampers [Accessed: 10 December 2025]

[17] MathWorks "Camera Calibrator: Estimate geometric parameters of a single camera", [online] Available at: https://www.mathworks.com/help/vision/ref/cameracalibrator-app.html [Accessed: 10 December 2025]

[18] MathWorks "estimateCameraParameters: Calibrate a single or stereo camera", [online] Available at: https://www.mathworks.com/help/vision/ref/estimatecameraparameters.html [Accessed: 10 December 2025]

[19] Sturm, P. "Pinhole Camera Model", In: Computer Vision, Springer, 2021, pp. 983–986. ISBN 978-3-030-63415-5 https://doi.org/10.1007/978-3-030-63416-2_472

[20] Drap, P., Lefèvre, J. "An Exact Formula for Calculating Inverse Radial Lens Distortions", Sensors, 16(6), 807, 2016. https://doi.org/10.3390/s16060807

[21] MathWorks "What Is Camera Calibration?", [online] Available at: https://www.mathworks.com/help/vision/ug/camera-calibration.html [Accessed: 10 December 2025]

[22] Zhang, Z. "A flexible new technique for camera calibration", IEEE Transactions on Pattern Analysis and Machine Intelligence, 22(11), pp.1330–1334, 2000. https://doi.org/10.1109/34.888718

[23] MathWorks "Matlab, (R2021b)", MathWorks, [Computer program] Available at: https://ch.mathworks.com/products/matlab.html?s_tid=hp_ff_p_matlab [Accessed: 10 December 2025]

[24] MathWorks "undistortImage: Correct image for lens distortion", [online] Available at: https://www.mathworks.com/help/vision/ref/undistortimage.html [Accessed: 10 December 2025]

[25] Atherton, T. J., Kerbyson, D. J. "Size invariant circle detection", Image and Vision Computing, 17(11), pp. 795–803, 1999. https://doi.org/10.1016/S0262-8856(98)00160-7

[26] Duda, R. O., Hart, P. E. "Use of the Hough transformation to detect lines and curves in pictures", Communications of the ACM, 15(1), pp. 11–15, 1972. https://doi.org/10.1145/361237.361242

[27] MathWorks "imfindcircles: Find circles using circular Hough transform", [online] Available at: https://www.mathworks.com/help/images/ref/imfindcircles.html [Accessed: 10 December 2025]

[28] MathWorks "mldivide, \: Solve systems of linear equations $Ax = B$ for x", [computer program] Available at: https://www.mathworks.com/help/matlab/ref/double.mldivide.html?s_tid=srchtitle_support_results_1_mldivide%2C%2520%5C%3A%2520Solve%2520systems%2520of%2520linear%2520equations%2520Ax%2520 [Accessed: 10 December 2025]

[29] MathWorks "atan2: Four-quadrant inverse tangent", [online] Available at: https://www.mathworks.com/help/matlab/ref/double.atan2.html [Accessed: 10 December 2025]

[30] MathWorks "unwrap: Shift phase angles", [online]. Available at: https://www.mathworks.com/help/matlab/ref/unwrap.html [Accessed: 10 December 2025]

[31] MathWorks "medfilt1: 1-D median filtering", [online]. Available at: https://www.mathworks.com/help/signal/ref/medfilt1.html [Accessed: 10 December 2025]

[32] Cherepanov, G. P. "Theory of rolling: Solution of the Coulomb problem", Journal of Applied Mechanics and Technical Physics, 55, pp. 182–189, 2014. https://doi.org/10.1134/S0021894414010210

[33] Kawulok, M., Pospisil, S. "Analysis of Damping of a Ball Absorber from Experimentally Obtained Data", Procedia Structural Integrity, 73, pp. 51–57, 2025. https://doi.org/10.1016/j.prostr.2025.10.009

[34] MathWorks "ode45: Solve nonstiff differential equations — medium order method", [online] Available at: https://www.mathworks.com/help/matlab/ref/ode45.html [Accessed: 10 December 2025]

[35] MathWorks "fmincon: Find minimum of constrained nonlinear multivariable function", [online] Available at: https://www.mathworks.com/help/optim/ug/fmincon.html [Accessed: 10 December 2025]